Wrinkling crystallography on spherical surfaces

Miha Brojan[a,1], Denis Terwagne[b,2], Romain Lagrange[c], and Pedro M. Reis[a,b,3]

Departments of [a]Mechanical Engineering, [b]Civil and Environmental Engineering, and [c]Mathematics, Massachusetts Institute of Technology, Cambridge, MA 02139

Edited by Howard A. Stone, Princeton University, Princeton, NJ, and approved November 24, 2014 (received for review June 19, 2014)

We present the results of an experimental investigation on the crystallography of the dimpled patterns obtained through wrinkling of a curved elastic system. Our macroscopic samples comprise a thin hemispherical shell bound to an equally curved compliant substrate. Under compression, a crystalline pattern of dimples self-organizes on the surface of the shell. Stresses are relaxed by both out-of-surface buckling and the emergence of defects in the quasi-hexagonal pattern. Three-dimensional scanning is used to digitize the topography. Regarding the dimples as point-like packing units produces spherical Voronoi tessellations with cells that are polydisperse and distorted, away from their regular shapes. We analyze the structure of crystalline defects, as a function of system size. Disclinations are observed and, above a threshold value, dislocations proliferate rapidly with system size. Our samples exhibit striking similarities with other curved crystals of charged particles and colloids. Differences are also found and attributed to the far-from-equilibrium nature of our patterns due to the random and initially frozen material imperfections which act as nucleation points, the presence of a physical boundary which represents an additional source of stress, and the inability of dimples to rearrange during crystallization. Even if we do not have access to the exact form of the interdimple interaction, our experiments suggest a broader generality of previous results of curved crystallography and their robustness on the details of the interaction potential. Furthermore, our findings open the door to future studies on curved crystals far from equilibrium.

mechanical instabilities | curved surfaces | pattern formation | packing | defects

The classic design of a soccer ball, with its 20 hexagonal (white) patches interspersed with 12 (black) pentagons, the buckminsterfullerene C_{60} (1), virus capsules (2), colloidosomes (3), and geodesic architectural domes (4) are all examples of crystalline packings on spherical surfaces. In contrast with crystals on flat surfaces, these structures cannot be constructed from a tiling of hexagons alone. Instead, disclinations—nonhexagonal elements such as the 12 pentagons on a soccer ball—are required by topology (5, 6), which constrains how the crystal order must comply with the geometry of the underlying surface. For example, seeding a hexagonal crystal with a pentagon (fivefold disclination) disrupts the perfect hexagonal symmetry and introduces a localized stress concentrator, which can be relaxed through out-of-plane deformation with positive Gaussian curvature (7, 8). Likewise, a heptagon (sevenfold disclination) induces a disturbance with negative Gaussian curvature.

An example of a physical realization of curved crystals is found in experiments on colloidal emulsions, where equally charged particles self-organize at the curved interface of two immiscible liquids (3, 9–11). These experiments build upon a wealth of previous theoretical and numerical investigations, as reviewed by Bowick and Giomi (12). For small system sizes, similarly to the soccer ball above, the "simplest" spherical crystals have exactly 12, fivefold disclinations, located at the vertices of a regular icosahedron (13). When the number of particles is sufficiently large, additional defects known as dislocations (5–7 disclination dipoles, which are not required by topology) emerge and break the translational order and lower the energy of the crystal more efficiently than pentagons alone (14, 15). In spherical packings with large number of particles, dislocations typically connect into linear chains to form scars (16) (strings of dislocations attached to a pentagonal disclination) and pleats (10) (strings of dislocations), which in contrast with flat space, start and terminate within the crystal (16). It is therefore organized collections of dislocations, rather than disclinations or isolated dislocations, that predominantly screen curvature in large systems. Disclinations, dislocations, and chains of dislocations interact not only with each other (e.g., through elasticity of the crystal), but also with the curvature of the substrate by a geometric potential that depends on the particular type of defect (17). Their total number and arrangement is primarily dictated by energetics, in addition to the topological constraints on the number of excess disclinations. The challenge in rationalizing these systems is enhanced by the fact that the number of metastable states grows exponentially with system size (18).

Crystallography on curved surfaces has also been considered in the context of deformable elastic membranes with internal crystalline order (8, 12). Elastic stresses in membranes, adhered to curved substrates (19–21), can be relaxed either by (*i*) out-of-surface buckling through wrinkling for compliant substrates, or (*ii*) the in-surface proliferation of topological defects for rigid substrates. For example, out-of-plane deformations in free-standing graphene sheets have been directly linked to energy minimization in the neighborhood of topological defects (22).

Here, we study a macroscopic model system in which a curved crystal arises from the wrinkling of a hemispherical shell bound to an equally curved compliant substrate (schematic in Fig. 1*A*). The dimpled pattern (Fig. 1*B*) self-organizes from an originally smooth surface when the sample is compressed and eventually buckles to relax the stress induced by depressurizing an undersurface cavity. Profilometry through laser scanning provides access to the topography of the patterns (Fig. 1*D*). From the positions of dimple centers, we construct spherical Voronoi tessellations (Fig. 1*E*) and find a striking agreement between the

Significance

Curved crystals cannot comprise hexagons alone; additional defects are required by both topology and energetics that depend on the system size. These constraints are present in systems as diverse as virus capsules, soccer balls, and geodesic domes. In this paper, we study the structure of defects of the crystalline dimpled patterns that self-organize through curved wrinkling on a thin elastic shell bound to a compliant substrate. The dimples are treated as point-like packing units, even if the shell is a continuum. Our results provide quantitative evidence that our macroscopic wrinkling system can be mapped into and described within the framework of curved crystallography, albeit with some important differences attributed to the far-from-equilibrium nature of our patterns.

Author contributions: M.B. and P.M.R. designed research; M.B., D.T., R.L., and P.M.R. performed research; M.B. and R.L. contributed new reagents/analytic tools; M.B., D.T., and P.M.R. analyzed data; and M.B. and P.M.R. wrote the paper.

The authors declare no conflict of interest.

This article is a PNAS Direct Submission.

[1]Present address: Faculty of Mechanical Engineering, University of Ljubljana, SI-1000 Ljubljana, Slovenia.

[2]Present address: Faculté des Sciences, Université Libre de Bruxelles (ULB), Bruxelles 1050, Belgium.

[3]To whom correspondence should be addressed. Email: preis@mit.edu.

www.pnas.org/cgi/doi/10.1073/pnas.1411559112

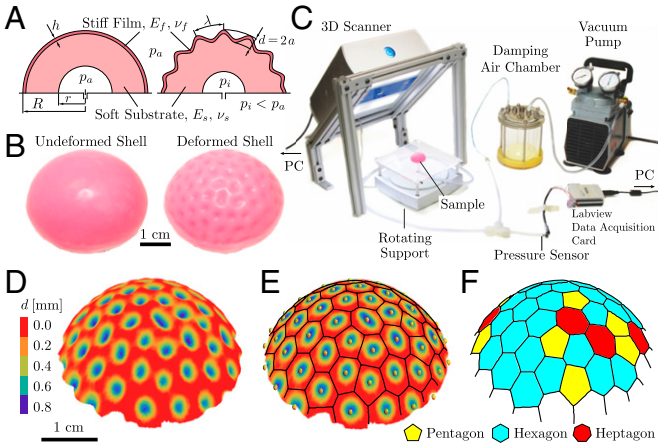

Fig. 1. Wrinkling patterns on hemispherical samples. (*A*) Schematic diagram of the setup. (*B*) Experimental sample: PDMS shell (radius $R = 20.0$ mm, thickness $h = 0.53 \pm 0.05$ mm, Young modulus $E_f = 2.10$ MPa, Poisson ration $\nu_f \approx 0.5$) adhered to a VPS substrate ($E_s = 0.23$ MPa, $\nu_s \approx 0.5$, radius of cavity, $r = 9.5$ mm). Undeformed configuration (at $\Delta p = 0$) and wrinkled pattern (at $\Delta p = 76.4$ kPa) with characteristic wavelength, $\lambda = 4.83 \pm 0.45$ mm (uncertainty is SD of all dimples). (*C*) Experimental apparatus: 3D scanner, pneumatic system, and pressure data acquisition system. (*D*) Surface profile of dimpled pattern. (*E*) Skeleton of the spherical Voronoi construction (black lines) obtained from the centers of the dimples (yellow circles), superposed on surface profile. (*F*) Voronoi tessellation, color coded according to the coordination number.

Voronoi construction and the network of ridges of the experimental pattern. We therefore regard the dimples as (point-like) packing units that repel one another, due to storage of elastic strain energy, which themselves form a continuum elastic shell. As such, we study the nucleation process and quantify the defect structure of our wrinkling patterns (Fig. 1*F*). By drawing analogies with the packing of particles on curved surfaces, we find that our system relaxes stresses both by out-of-surface buckling through the formation of arrays of dimples, and by simultaneously developing topological defects in these patterns. Moreover, our macroscopic system is found to mimic many of the identifying features of other curved crystals (9, 10) (a priori far from obvious, given the difference of the underlying physics), despite some important differences in the morphology of defects and their rapid growth with system size that we attribute to the far-from-equilibrium nature of our system.

Wrinkling on Curved Surfaces: Our Experiments

We have recently introduced an experimental system to study wrinkling on curved surfaces, as smart morphable surfaces for aerodynamic drag reduction (23). Periodic wrinkling patterns emerge from the mechanical instability of a thin stiff film adhered to a soft foundation under compression. Whereas wrinkling of flat-plate–substrate systems is well understood (24–26), investigations of the curved counterpart have been mostly limited to numerics (26–28) and microscopic experiments (29, 30), where it is challenging to independently tune the control parameters.

Our centimetric hemispherical samples (radius R) comprise a thin–stiff shell adhered to a soft–thick substrate and were fabricated out of silicone-based elastomers using rapid prototyping techniques (see the schematic in Fig. 1*A* and *Materials and Methods* for the fabrication details and ranges of parameters). Using the pneumatic apparatus shown in Fig. 1*C*, a pressure difference $\Delta p = p_a - p_i$ can be set up between the outside atmospheric pressure, p_a and p_i, inside the undersurface cavity of radius r. Above a critical load, an undulatory wrinkling pattern emerges from the originally smooth shell (Fig. 1*B*), with a characteristic wrinkling wavelength λ dictated by the combination of geometric and material properties of the film and substrate.

We have found (23) that the curvature of the substrate leaves the wrinkling length scale unchanged, compared with that predicted for flat infinite substrates (25),

$$\lambda = 2\pi h \left[\frac{1-\nu_s^2}{1-\nu_f^2} \frac{E_f}{3E_s} \right]^{1/3}, \qquad [1]$$

where h is the thickness of the film, and E_f, ν_f and E_s, ν_s are the Young's moduli and Poisson's ratios of the film and substrate, respectively. However, curvature of the substrate (23, 29, 30) and the level of overstress (29, 31) can affect the pattern selection mode. For $h/R \lesssim 0.01$ (and low overstress) labyrinthine patterns were found (23). On the other hand, for $h/R \gtrsim 0.01$ we observed dimpled patterns that pack in a hexagonal-like crystal structure (Fig. 1*B*). From here on, we focus exclusively on these dimpled patterns to characterize and analyze their crystallographic structure.

Three-Dimensional Scanning and Spherical Voronoi Construction

The full 3D surface profile of the samples was digitized using a laser scanner (Fig. 1*C*). In Fig. 1*D*, we present the resulting topographic map of the radial surface depth d (measured from the outer spherical surface) for a representative fully developed dimpled pattern. Dimples (blue regions) are crater-like depressions, separated by ridges (red regions). Using an image processing algorithm developed in-house (*Materials and Methods*), we identify the spherical coordinates of the centers (local minima of d) of all of the dimples in a sample (yellow markers superposed in Fig. 1*E*). With the coordinates of the dimple locations at hand, we then construct a spherical Voronoi tessellation (black lines superposed in Fig. 1*E*).

It is remarkable that the skeleton provided by the Voronoi construction accurately delineates the underlying network of ridges of the experimental pattern (Fig. 1*E*), suggesting that each dimple is well represented by the corresponding Voronoi cell. As such, the dimples can be regarded as quasi-particles with characteristic interparticle distance λ (given by Eq. **1**). Because the system is under compression, these quasi-particles repel one another through an elastic potential, the precise characterization of which would require a detailed theoretical description that goes beyond the scope of our experimental work. We regard our dimpled patterns as self-organized tilings of a well-defined individual unit—the dimple—that packs into a quasi-hexagonal arrangement constrained by the underlying curved surface. In Fig. 1*F*, we show an example of the output of our procedure: a Voronoi tiling, where each dimple is replaced by the corresponding Voronoi cell. This representation will be used extensively below, to analyze our patterns.

Crystallization of the Dimpled Patterns

We first turn to the process of nucleation and then describe the structure of the fully developed crystalline patterns.

Nucleation. In Fig. 2 *A–H* we present snapshots (top views) of one of our samples during a loading and unloading cycle, starting from a spherical (undeformed) configuration at $\Delta p = 0$ kPa, loading it up to a maximum of $\Delta p = 76.4$ kPa, and then unloading to $\Delta p = 6.5$ kPa (the experimental uncertainty of all pressure measurements is ± 0.12 kPa). This particular sample has radius $R = 20.0$ mm and a characteristic dimple size of $\lambda = 4.40 \pm 0.60$ mm (set by $E_f = 2.10 \pm 0.11$ MPa, $E_s = 0.23 \pm 0.01$ MPa, $\nu_f = \nu_s \approx 0.5$, and $h = 0.48 \pm 0.07$ mm that is determined from Eq. **1**, *Materials and Methods*).

A few dimples first emerge, nonuniformly (Fig. 2*A*, $\Delta p = 6.5$ kPa). These are small regions of the initially smooth shell that buckle inward and eventually act as nucleation sites from which the rest of the pattern progressively grows with Δp (e.g., Fig. 2 *B* and *C*, $\Delta p = 13.1$ kPa and 23.4 kPa, respectively). The front of the crystalline phase spreads into the undimpled portions of the shell, until full coverage of the hemisphere is attained (Fig. 2*D*,

$\Delta p = 40.3$ kPa). Beyond this point, and up to $\Delta p = 76.4$ kPa, the maximum depressurization explored (Fig. 2*E*), there is no rearrangement of the dimples. The unloading path is, however, qualitatively different. Gradually decreasing the differential pressure from $\Delta p = 76.4$ kPa results in patterns whose morphology remains approximately unchanged (Fig. 2 *E–G*). Back at $\Delta p = 6.5$ kPa, the configuration in Fig. 2*H* is remarkably different from that of Fig. 2*A*, which is significant of hysteresis.

In Fig. 2*I*, we quantify this hysteretic behavior by plotting the average depth of dimples d as a function of Δp. For $\Delta p < 40.3$ kPa (partial coverage of the sample), there are three distinct paths in the mechanical response: one for the first loading ramp and the other two for subsequent unloading and loading cycles. All paths converge above $\Delta p \approx 40$ kPa (beyond which the full sample is crystalline), and up to the maximum $\Delta p \approx 75$ kPa explored. Note that our system is elastic, the viscosity of the elastomers we use is negligible, and there is no delamination between the film and substrate. As such, we attribute this hysteretic behavior to the series of multiple snap-buckling events that must occur on the initially smooth spherical shell for each of the individual dimples to form.

We highlight that the position of each dimple remains fixed after nucleation and throughout the evolution of the pattern (Fig. 2 *A–D*, $0 < \Delta p$[kPa] < 40.3). Moreover, repeating the experiments with the same sample leads to identical patterns. The loci of nucleation occur presumably at regions of "frozen" material imperfections (e.g., due to small air bubbles trapped in the elastomer during curing). The appearance of subsequent dimples propagates from these nucleation sites, which we therefore refer to as anchor dimples, until the full surface crystallizes. Interestingly, the depth of these anchor dimples does not differ significantly ($\lesssim 5\%$) from the average dimple depth once the pattern is fully developed. The mechanism by which anchor dimples emerge is still uncertain. However, based on the work of Paulose and Nelson (32), we speculate that frozen imperfections may generate small soft regions on the cap, which can snap-buckle.

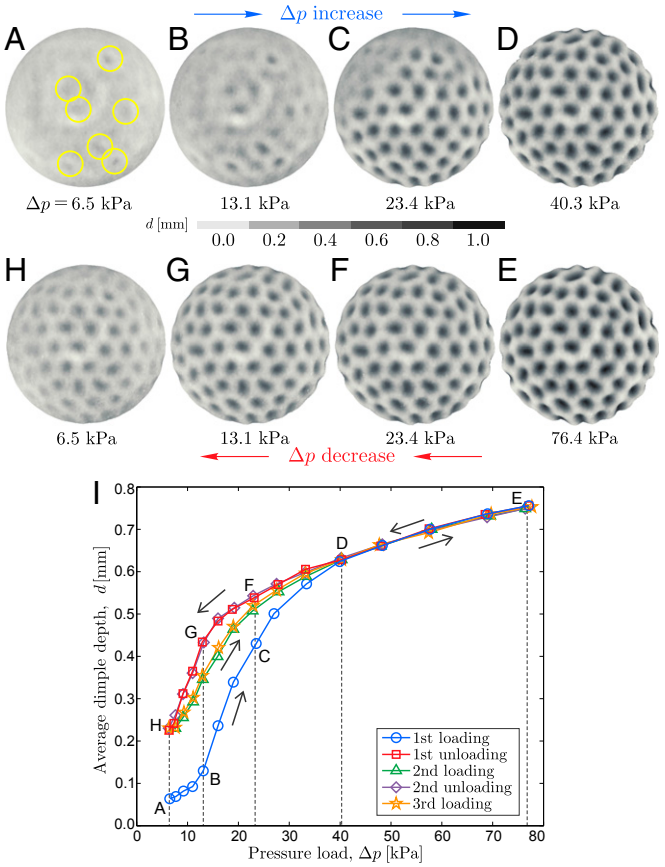

Fig. 2. Crystallization of the dimpled patterns. (*A–H*) Top-view snapshots of the surface profile during a loading–unloading cycle. (*A–E*) Loading with increasing $\Delta p = (6.5, 13.2, 23.4, 40.3, 76.4)$ kPa. (*E–H*) Unloading at the same values of Δp. Anchor dimples in *A* are marked with circles. (*I*) Experimental measurements of the average dimple depth d as a function of Δp. Three loading paths (increasing Δp) and two unloading paths (decreasing Δp) are shown. Solid lines are guides to the eye and the labeled data points correspond to the patterns in *A–H*. The shell thickness is $h = 0.48 \pm 0.07$ and other parameters identical to Fig. 1.

Structure of the Crystalized Dimpled Patterns. We now make use of the Voronoi representation introduced above to further analyze the experimental patterns. In Fig. 3 *A–F* we show a series of examples of Voronoi tilings superimposed on top of the scanned data for samples with increasing values of R/λ, a measure of the relative system size, attained by changing the shell thickness in the range $0.23 < h$[mm] < 0.88 (which modifies λ through Eq. **1**), while keeping all other parameters fixed ($R = 20.0$ mm, $r = 9.5$ mm, and $E_f/E_s = 9.13$). Note that larger values of R/λ correspond to thinner shells because $\lambda \sim h$. Regions shaded in gray represent bands of dimples which were taken into account for identifying the coordination number (i.e., number of neighbors) of the dimples inside the solid green line, but otherwise omitted from further quantitative analysis. The coordination numbers of these border dimples are undetermined and they cannot be interpreted under our framework of packing of point-like units. The domain of interest is thus reduced from a hemisphere to a spherical cap.

For all samples in Fig. 3 *A–F*, the most prominent cells are hexagonal (in blue) as expected from crystallinity. As R/λ is increased, pentagonal and heptagonal defects (yellow and red, respectively) become more prominent. The "simplest" lattice structure is found for $R/\lambda = 2.21$ (Fig. 3*A*), representative of small system sizes, with seven hexagons and three isolated pentagonal disclinations. For $R/\lambda = 3.75$ (Fig. 3*B*), series of dislocation defects (5–7 disclination dipoles) appear, in addition to hexagons and isolated pentagons. This pattern comprises one isolated pentagonal disclination, two isolated dislocations, and two strings of dislocations which resemble a scar and a pleat. Note, however, that a true scar and pleat would start and terminate in the interior of the curved crystal (33), but in our case they often do so at the boundary. Still, the overall scenario in our experimental patterns is analogous to that found in other curved crystals (9–11). For even larger sample sizes (see Fig. 3 *D–F*, for $R/\lambda > 4.71$), there is a proliferation of more complex arrangements of defects with clusters, as well as strings of dislocations that are increasingly longer and branched. By contrast, branching of linear arrays of dislocations, as well as isolated dislocations in large system sizes, would not occur in crystals at equilibrium.

In Fig. 3*G*, we present the cap ratio α, the ratio between the area of the spherical cap that is analyzed and the area of the corresponding full sphere $4\pi R^2$, as a function of R/λ. As expected, α increases with R/λ; the relative size of the dimples decreases, and the required exclusion band is increasingly smaller. The sharp drop in α for $R/\lambda \gtrsim 6.5$, however, is due to a technical difficulty in our 3D scanning procedure that forced us to only acquire top-view scans for these samples with smaller dimples (instead of the full hemispherical surface obtained from the stitching of multiple perspectives, for $R/\lambda \lesssim 6.5$). The white annuli in Fig. 3 *E* and *F* represent the portions of the samples that were not scanned.

Polydispersity and Topology of Dimples. We proceed by quantifying the area of the Voronoi cells that underlies the crystalized dimpled patterns, as well as the topology of their tilings. For this, we consider statistical ensembles of the individual cells associated with each dimple, whose coordination number allows for their classification as pentagons, hexagons, or heptagons. By way of example, we focus on a set of nine samples ($R = 20.0$ mm, $E_f/E_s = 9.13$ and $\lambda = (3.07 \pm 0.10)$ mm; the uncertainty is the SD of the mean of the set), each with ~180 dimples.

Polydispersity is measured using the ratio $A^* = A_i/A_{\text{hex}}$, where A_i is the area of each Voronoi cell, and $A_{\text{hex}} = \sqrt{3}\lambda^2/2$ is the area

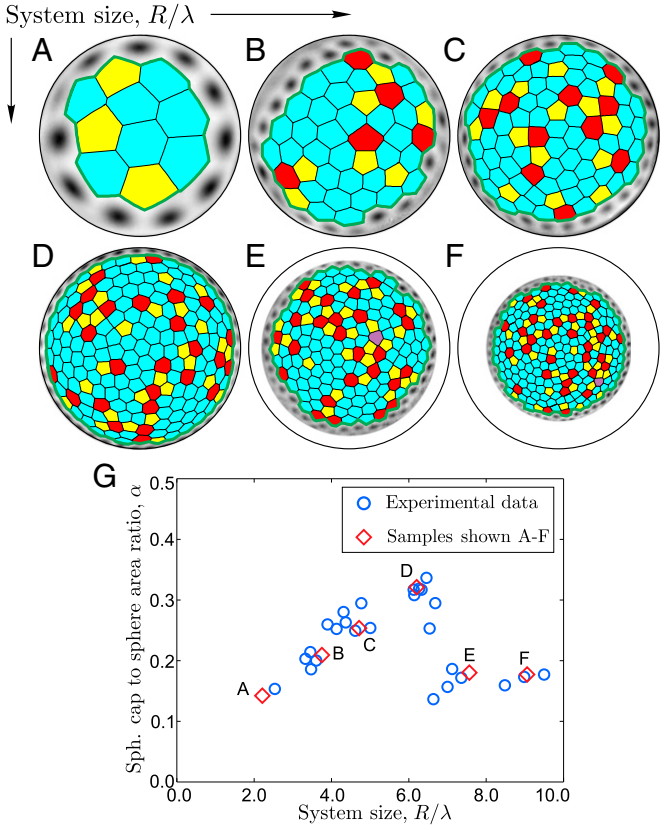

Fig. 3. Voronoi tessellations and structure of defects. (*A–F*) Top views of tilings superimposed on the scanned data with increasing values of dimensionless system size, $R/\lambda = (2.21, 3.75, 4.71, 6.20, 7.56, 9.06)$, respectively. Pentagonal, hexagonal, and heptagonal cells are colored in yellow, blue, and red, respectively. Physical edges (equators) of the shell samples are encircled black. Only the regions inside the pseudoboundary represented by the thick-solid green envelope were analyzed. Dimples outside this green boundary were not considered. The surface regions in the white annulus were not scanned. (*G*) Ratio between the area of a spherical cap and the area of the corresponding full sphere α as a function of R/λ. The samples from *A–F* are marked with red diamonds.

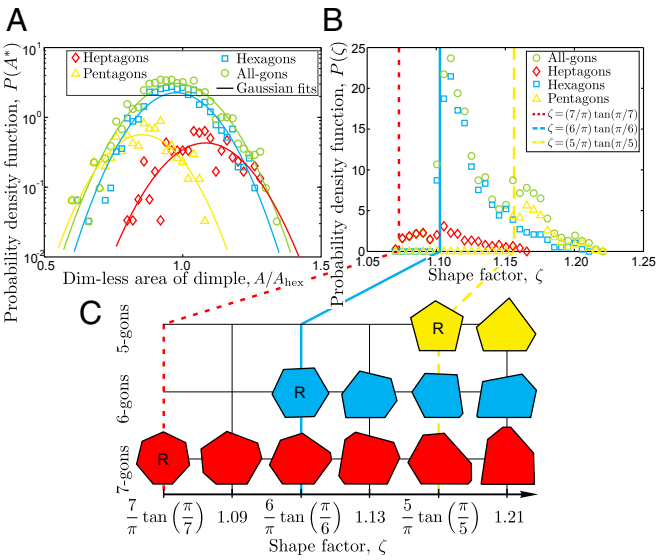

Fig. 4. Polydispersity and distortion of Voronoi cells. (*A*) Probability density function of dimensionless area of Voronoi cells A^*. Area of each cell is normalized by the area of regular hexagons, $A_{hex} = \sqrt{3}\lambda^2/2$, for a characteristic dimple size λ. Gaussian distribution fits are represented with solid lines. (*B*) PDF of shape factor ζ. Vertical lines located at the corresponding values for regular pentagons, hexagons, and heptagons, $\zeta_n = n/\pi\tan(\pi/n)$, with $n = 5$, 6, and 7, respectively. (*C*) Representative Voronoi cells for specific values of ζ. Regular polygons are marked with "R."

of a regular Euclidean hexagon with a distance λ (defined in Eq. **1**) between the parallel sides. A constant value of $A^* = 1$ for all cells would correspond to a perfectly monodisperse hexagonal pattern, which is, however, unattainable in a curved system. In Fig. 4*A*, we present the probability density function (PDF), $P(A^*)$, of all Voronoi cells in the ensemble. We find that $P(A^*)$ is well described by a Gaussian distribution, $P(A^*) = [1/(\sigma\sqrt{2\pi})]$ $\exp[-(A^* - \overline{A}^*)^2/(2\sigma^2)]$, with a mean $\overline{A}^* = 0.98$ and SD $\sigma = 0.12$. The near-unity value of $\overline{A}^*$ is indicative of the hexagonal crystalline packing but the significant SD conveys that the dimples are polydisperse. We have also classified the area of each cell according to its coordination number, A_7^*, A_6^*, and A_5^*, for heptagons, hexagons, and pentagons, respectively. The corresponding relative PDFs, normalized such that $\int_0^\infty P_7 dA_7^* + \int_0^\infty P_6 dA_6^* + \int_0^\infty P_5 dA_5^* = 1$ are also Gaussian distributed (see fits in Fig. 4*A*). Whereas $P_6(A_6^*)$ is still peaked near unity, $(\overline{A}_6^*, \sigma_6) = (0.99, 0.11)$, there is a splitting for the mean areas for heptagons and pentagons, $(\overline{A}_7^*, \sigma_7) = (1.07, 0.12)$ and $(\overline{A}_5^*, \sigma_5) = (0.88, 0.10)$, respectively. Note that this splitting occurs nearly symmetrically from $\overline{A}^*$. The high coefficients of variation, $\sigma_i/A_i^* \approx 11\%$, indicate a high degree of polydispersity for all families of cells.

In addition to polydispersity, we quantify the morphology of the Voronoi cells by measuring their shape factor, $\zeta = C_i^2/(4\pi A_i)$, where C_i and A_i are the perimeter and surface area of each cell, respectively (34, 35). This quantity accounts for both the topology and the level of distortion of each Voronoi cell. The shape factor is $\zeta = 1$ for a circle and $\zeta > 1$ for all other shapes. For example, regular pentagons, hexagons, and heptagons have $\zeta_n = n/\pi\tan(\pi/n)$ with $n = 5, 6$, and 7, respectively.

In Fig. 4*B*, we plot the PDF for shape factor of all cells, $P(\zeta)$. Similarly to $P(A^*)$ above, we also superpose the relative PDFs for the families of heptagons, hexagons, and pentagons, normalized such that $\int_1^\infty P_7 d\zeta_7 + \int_1^\infty P_6 d\zeta_6 + \int_1^\infty P_5 d\zeta_5 = 1$. The probability of finding a particular polygon peaks sharply after the value of shape factor that corresponds to its regular shape: $\zeta \approx 1.073, 1.103$, and 1.156 for regular heptagons, hexagons, and pentagons, respectively. After these peaks, the corresponding probabilities decrease but remain finite for an extended range of ζ. Moreover, the PDF for all cells $P(\zeta)$ is nonzero in the broad interval of shape factors $1.073 < \zeta < 1.299$, meaning that the tilings of our dimpled patterns consist of irregular Voronoi cells. To illustrate this spread, we show in Fig. 4*C* representative examples of cells obtained by sampling the PDFs at specific values of ζ, for each of the polygon families. For example, at $\zeta = 5/\pi\tan(\pi/5)$, the value for a regular pentagon, distorted hexagons, and heptagons are also found. Likewise, for a specific family, increasing ζ corresponds to increasingly more distorted polygons.

Quantification of the Defect Structure

Thus far, we have learned that the tilings of our dimpled patterns consist of polydisperse Voronoi cells, with a distribution of distorted polygons, away from their regular shapes. Whereas previous studies focused on more monodisperse systems (9, 10, 16), Euler's packing theorem is applicable to general tilings. As such, we follow an approach similar to that of refs. 9, 10 and quantify the defect structure versus system size R/λ for 32 samples in the range $2.09 < \lambda[\text{mm}] < 8.01$ $(0.23 < h[\text{mm}] < 0.88$, while fixing $R = 20$ mm and $E_f/E_s = 9.13)$.

Net Defect Charge. The topological charge $q = \pi s/3$ is commonly used to quantify defects of curved crystals (12), where the disclination charge,

$$s = 6 - Z, \quad [2]$$

is the deviation of the coordination number Z from that of a perfect hexagonal packing; $s = +1$ for a pentagon and $s = -1$ for a heptagon, i.e., $q = +\pi/3$ and $q = -\pi/3$, respectively. From the Gauss–Bonnet and Euler theorems (5, 6), it follows that, for any triangulation over a spherical surface, there exists a fixed topological constraint on the sum of these discrete charges (+12 on a sphere). We define the net topological charge for an ensemble of N_α lattice units on a spherical cap with area $4\pi R^2\alpha$ (the area ratio α was quantified in Fig. 3*G* for our samples) as

$$Q_\alpha = Q\alpha = \sum_i^{N_\alpha} q_i = 4\pi\alpha. \quad [3]$$

We now analyze our data following a procedure recently used for curved colloidal crystals (10). For a given sample, we measure the net defect charge Q_β of spherical "patches" of variable area (defined by the ratio β of their area with that of a sphere; Fig. 5*A*, *Inset*) up to the maximum possible cap allowed for that sample (Fig. 3*G*), such that $0 < \beta \leq \alpha$. Such a measurement includes both the effects of isolated disclinations and the polarization charge due to the nonuniform distribution of disclination dipoles [by analogy with electrostatics (10)]. In this procedure, the contribution to the polarization charge is accounted for by the cumulative counting when the boundary of the analyzed patches with increasing sizes dissects a pleat or a dislocation and adds toward the total topological charge, which would not occur for a full sample. In Fig. 5*A*, we plot this net defect charge as a function of the integrated Gaussian curvature, $\int GdA = 4\pi\beta$, of the patches ($G = 1/R^2$ in our spherical case) for multiple samples with different values of R/λ. The data are consistent with a linear relation between defect charge and integrated Gaussian curvature, with unit slope, that was likewise previously observed on curved crystals, albeit with a significant level of scatter that is also consistent with the experiments in ref. 10. It is striking that, despite the differences in the underlying physics of the two curved systems, our macroscopic wrinkling patterns and colloidal packings can be analyzed and interpreted similarly.

Average Coordination Number. Given the scatter in Q_β, we turn to the average coordination number $\overline{Z} = (1/N)\sum_{i=1}^{N} Z_i$ for a tiling with N dimples. However, before quantifying $\overline{Z}$, we step back and consider the number of dimples N_α in our samples, as a function of R/λ. For large systems, where R is large compared with λ and the hexagonal cells far outnumber disclinations, we assume that the area of each dimple is $A_i \approx (\sqrt{3}/2)\lambda^2$. This is supported by the above finding that $A^* \approx 1$ (Fig. 4*A*). In turn, the total number of dimples on a spherical cap is $N_\alpha \approx 4\pi R^2\alpha/A_i$, which yields

$$N_\alpha \approx \frac{8\pi\alpha}{\sqrt{3}}\left(\frac{R}{\lambda}\right)^2. \quad [4]$$

In Fig. 5*B*, we plot the experimental measurements for N_α/α (extrapolated to a sphere), which are in excellent agreement with Eq. **4** (solid line).

Toward determining $\overline{Z}$, the average net topological charge per lattice unit is $Q_\alpha/N_\alpha = (1/N_\alpha)\sum_{i=1}^{N_\alpha} q_i = 4\pi\alpha/N_\alpha$, through Eq. **3**. Combining this result with the definition of q and making use of Eqs. **2** and **4** gives

$$\overline{Z} \approx 6\left[1 - \frac{\sqrt{3}}{4\pi}\left(\frac{R}{\lambda}\right)^{-2}\right]. \quad [5]$$

A more general version of Eq. **5** was provided by Nelson (7) but, for completeness, we have reproduced the argument applied specifically to our system.

In Fig. 5*C*, we plot $\overline{Z}$ measured directly from our samples, as a function of system size, finding that the data are in very good agreement with Eq. **5**. A perfect hexagonal packing (e.g., on a plane or a cylinder) would have $\overline{Z} = 6$, but the presence of defects forces $\overline{Z} < 6$. Moreover, the deviations from the planar result (horizontal dashed line in Fig. 5*C*, at $\overline{Z} = 6$) become more pronounced for smaller systems, as the relative importance of pentagonal disclination increases.

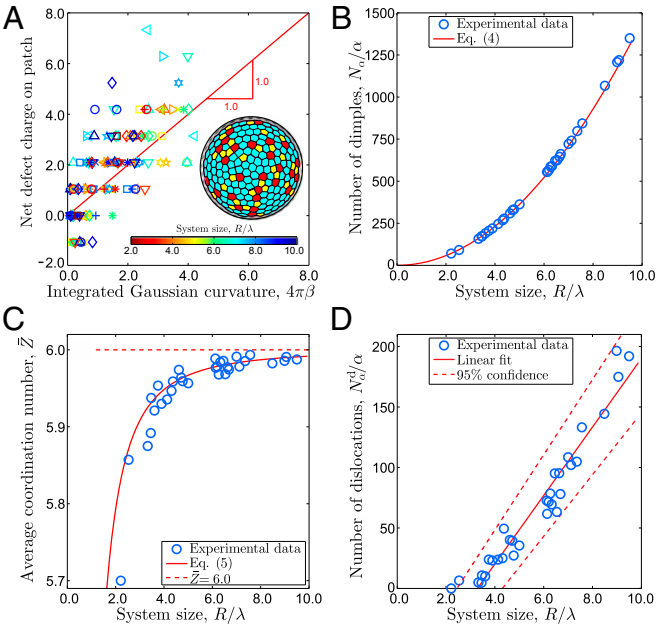

Fig. 5. Quantification of defects. (*A*) Net defect charge (sum of disclination and polarization charges) on spherical patches of variable size (within a given sample, with a patch-to-sphere area ratio in the range $0 < \beta \leq \alpha$), as a function of integrated Gaussian curvature $4\pi\beta$. The adjacent color bar represents system size R/λ. Different markers are used to better identify different data points. (*Inset*) Purple lines represent the edges of the analyzed spherical patches, with increasing values of β. (*B*) Number of counted dimples N_α/α (extrapolated to a full sphere) vs. R/λ. Solid line is prediction from Eq. **4**. (*C*) Average coordination number $\overline{Z}$ as a function of R/λ. Solid line is prediction from Eq. **5**, dashed line is $\overline{Z} = 6$. (*D*) Number of dislocations N_α^d/α (extrapolated to a full sphere) as a function of R/λ. The solid line is a linear fit with slope 28.3 (±2.8 SD) and intercept with horizontal axis at $(R/\lambda)_c = 3.2$ (±0.7 SD.). See *Materials and Methods* for details on the geometric and material properties of the 32 samples used.

Number of Dislocations. Further, we quantify the total number of dislocations N_α^d for our dimpled patterns. In Fig. 5*D*, we plot N_α^d/α (experimental value for the spherical cap extrapolated to a sphere) as a function of R/λ. We find that the number of dislocations grows linearly with system size, $N_\alpha^d/\alpha \sim (R/\lambda)$, with a slope $m = 28.3 \pm 2.8$ and an intercept with the horizontal axis, $(R/\lambda)_c = 3.2 \pm 0.7$. This finite value of $(R/\lambda)_c$ is significant of a threshold system size for the onset of dislocations, below which only isolated, topologically required disclinations are found. Through Eq. **4**, this translates into a sample with a threshold number of dimples, $N_c \approx 150$ (after extrapolating to a sphere using α).

Remarkably, this scenario is qualitatively identical to that of Bausch et al. (9), who found $(R/\lambda)_c \approx 5$, for a system of colloidal particles on the surface of spherical oil droplets which had previously been predicted by theory (16, 33), and a critical system size of $N_c \approx 360$ particles. These similarities are despite the fact that the system of Bausch et al. (9) was microscopic, whereas ours is macroscopic, and in the measurement procedure for the number of dislocations, they took the average number of dislocations per chain, detached from the boundary, whereas we used all chains because they regularly emanate from the boundary.

Discussion and Conclusion

We have introduced a macroscopic experimental model system where a curved crystalline pattern of dimples self-organizes from the wrinkling of an originally smooth thin elastic shell. The system

relaxes stresses both by out-of-surface buckling through the formation of arrays of dimples, and by simultaneously developing defects as nonhexagonal dimples in the otherwise hexagonal patterns. Direct parallels were established between the structure of defects in our system and previous studies on the packing of charged particles on curved surfaces (14–16) and curved colloidal crystals (9, 10), despite the differences in the underlying physics. These similarities include the ability to treat the dimples as point-like units, the use of Voronoi tessellation to characterize their packing, as well as the presence of disclinations and, above a threshold system size, the prominent growth of the number of dislocations to screen the underlying curvature. There are however few important distinctions. We observe dislocations that form branched arrays and clusters and proliferate more rapidly than in curved colloidal crystals (9, 16), and with a different threshold value of system size. We speculate that these differences may be attributed to the fact that we have a different repulsive potential and our system is far from equilibrium due to the random and initially frozen material imperfections that nucleate the pattern, as well as the inability for the dimples to rearrange during crystallization. Consequently, these constraints prevent our system from exploring phase space and lead to additional frustration that increases disorder.

The interaction potential between neighboring dimples in our system is still unknown. However, Bowick et al. (33) find that potentials of the form $1/r^{\gamma}$, with $0<\gamma<2$, lead to similar defect structures. This provides a possible explanation as to why, despite the different nature of the interdimple elastic potential in our wrinkling system, we still find many of the general features of other 2D curved crystals. We hope that our experimental results will instigate further studies of curved crystallography in more complex geometries (e.g., on a torus) and in instances of far from equilibrium (e.g., with anchoring imperfections), which remain largely unexplored.

Materials and Methods

Fabrication of Samples. We manufactured 32 hemispherical samples, made of silicone-based elastomers, polydimethylsiloxane (PDMS) and vinylpolysiloxane (VPS), for the film and the substrate, respectively, using a protocol that was described previously (23). First, a thin outer shell was made by coating a previously vacuum-formed polystyrene mold with the desired radius. The coating process included wetting the surface of the mold and then draining the excess polymer by gravity. A balance between gravity, viscosity, surface tension, and polymerization rate yielded shells of constant thickness (to within $\sim 10\%$ variation). This process could be repeated multiple times to obtain thicker shells. Next, pouring the VPS into the mold (now containing the fully polymerized thin shell) produced the soft foundation. Immediately after the elastomer was cast, the mold was covered with an acrylic plate containing a spherical 3D printed part, which produced the undersurface cavity. Upon curing and demolding, the samples were stored in a ventilated area for 1 wk to fully cure before the experimental tests were performed.

Material and Geometric Properties. The mechanical properties of PDMS and VPS were measured on cylindrical specimens subjected to uniaxial compression using a material testing machine (Zwick). We found a linear stress–strain response of these materials within the levels of compression relevant to our experiments. The ratio between the Young moduli of the film and substrate could be controlled within the range $1.0 \le E_f/E_s \le 162.0$ (for different mixtures of the base and curing agents), whereas the Poisson ratios of the film and the substrate was $\nu_f = \nu_s \approx 0.5$. The thickness of the shell was varied in the range $0.23 < h[\text{mm}] < 0.88$, while fixing the radii of shell, $R = 20.0$ mm, and the cavity, $r = 9.5$ mm.

Three-Dimensional Scanning and Image Analysis. The surface topography of the dimpled patterns on the hemispherical samples was digitized using a 3D laser scanner (NextEngine) and the resulting cloud of points was postprocessed using MATLAB. The Cartesian coordinates (x,y,z) of each point were converted into spherical coordinates (ϕ,θ,ρ), where ϕ and θ are the azimuth and polar angles, and ρ is the radial distance from each point to the centroid of the sphere that best fits the outer surface of the sample. In our analysis we used a stitched combination of (ϕ,θ,ρ) and (x,y,ρ) coordinate representation to address the distortion of the $\rho(\phi,\theta)$ map at small polar angles. A gray-scale image using ρ as the field variable was thresholded into black and white binaries, corresponding to valleys of the dimples and the ridges, respectively. Determining the centroids of all black blobs yielded the coordinates of the centers of all dimples, from which the final Voronoi tessellation was constructed.

ACKNOWLEDGMENTS. The authors thank A. Bresson for help with preliminary experiments. P.M.R. acknowledges support from MIT's Charles E. Reed faculty initiative fund, the National Science Foundation, CMMI-1351449 Faculty Early Career Development (CAREER) Program, and is grateful to U. Deusto for hospitality. M.B. thanks the Fulbright Program. D.T. thanks the Belgian American Education Foundation (BAEF), the Fulbright Program, and the Wallonie-Bruxelles International Excellence Grant WBI World.

1. Kroto HW, Heath JR, O'Brien SC, Curl RF, Smalley RE (1985) C60: Buckminsterfullerene. *Nature* 318:162–163.
2. Caspar DLD, Klug A (1962) Physical principles in the construction of regular viruses. Cold Spring Harbor Symposium 27:1–24.
3. Dinsmore AD, et al. (2002) Colloidosomes: Selectively permeable capsules composed of colloidal particles. *Science* 298(5595):1006–1009.
4. Fuller R (1954) Building construction. US Patent 2,682,235.
5. Sadoc JF, Mosseri R (1999) *Geometrical Frustration* (Cambridge Univ Press, Cambridge, UK).
6. Richeson DS (2008) *Euler's Gem: The Polyhedron Formula and the Birth of Topology* (Princeton Univ Press, Princeton, NJ).
7. Nelson DR (1983) Order, frustration, and defects in liquids and glasses. *Phys Rev B* 28(10):5515–5535.
8. Seung HS, Nelson DR (1988) Defects in flexible membranes with crystalline order. *Phys Rev A* 38(2):1005–1018.
9. Bausch AR, et al. (2003) Grain boundary scars and spherical crystallography. *Science* 299(5613):1716–1718.
10. Irvine WTM, Vitelli V, Chaikin PM (2010) Pleats in crystals on curved surfaces. *Nature* 468(7326):947–951.
11. Irvine WTM, Bowick MJ, Chaikin PM (2012) Fractionalization of interstitials in curved colloidal crystals. *Nat Mater* 11(11):948–951.
12. Bowick MJ, Giomi L (2009) Two-dimensional matter: Order, curvature and defects. *Adv Phys* 58(5):449–563.
13. Dodgson MJW (1996) Investigation on the ground states of a model thin film superconductor on a sphere. *J Phys Math Gen* 29(10):2499–2508.
14. Dodgson MJW, Moore MA (1997) Vortices in a thin-film superconductor with a spherical geometry. *Phys Rev B* 55(6):3816–3831.
15. Perez-Garrido A, Dodgson JW, Moore MA (1997) Influence of dislocations in Thomson's Problem. *Phys Rev B* 56(7):3640–3643.
16. Bowick MJ, Nelson DR, Travesset A (2000) Interacting topological defects on frozen topographies. *Phys Rev B* 62(13):8738–8751.
17. Vitelli V, Lucks JB, Nelson DR (2006) Crystallography on curved surfaces. *Proc Natl Acad Sci USA* 103(33):12323–12328.
18. Erber T, Hockney GM (1991) Equilibrium configurations of N equal charges on a sphere. *J Phys Math Gen* 24(23):1369–1377.
19. Grason GM, Davidovitch B (2013) Universal collapse of stress and wrinkle-to-scar transition in spherically confined crystalline sheets. *Proc Natl Acad Sci USA* 110(32):12893–12898.
20. Funkhouser CM, Sknepnek R, de la Cruz MO (2013) Topological defects in the buckling of elastic membranes. *Soft Matter* 9:60–68.
21. Azadi A, Grason GM (2014) Emergent structure of multidislocation ground states in curved crystals. *Phys Rev Lett* 112(22):225502.
22. Zhang T, Li X, Ga H (2014) Defects controlled wrinkling and topological design in graphene. *J Mech Phys Solids* 67:2–13.
23. Terwagne D, Brojan M, Reis PM (2014) Smart morphable surfaces for aerodynamic drag control. *Adv Mater* 26(38):6608–6611.
24. Bowden N, Brittain S, Evans AG, Hutchinson JW (1998) Spontaneous formation of ordered structures in thin films of metals supported on an elastomeric polymer. *Nature* 393:146–149.
25. Chen X, Hutchinson JW (2004) Herringbone buckling patterns of compressed thin films on compliant substrates. *J Appl Mech* 71:597–603.
26. Li B, Cao YP, Feng XQ, Gao H (2012) Mechanics of morphological instabilities and surface wrinkling in soft materials: A review. *Soft Matter* 8:5728–5745.
27. Yin J, Cao Z, Li C, Sheinman I, Chen X (2008) Stress-driven buckling patterns in spheroidal core/shell structures. *Proc Natl Acad Sci USA* 105(49):19132–19135.
28. Li B, Jia F, Cao YP, Feng XQ, Gao H (2011) Surface wrinkling patterns on a core-shell soft sphere. *Phys Rev Lett* 106(23):234301.
29. Cai S, Breid D, Crosby AJ, Suo Z, Hutchinson JW (2011) Periodic patterns and energy states of buckled films on compliant substrates. *J Mech Phys Solids* 59:1094–1114.
30. Breid D, Crosby AJ (2013) Curvature-controlled wrinkle morphologies. *Soft Matter* 9:3624–3630.
31. Audoly B, Boudaoud A (2008) Buckling of a stiff film bound to a compliant substrate - Part I: Formulation, linear stability of cylindrical patterns, secondary bifurcations. *J Mech Phys Solids* 56:2401–2421.
32. Paulose J, Nelson DR (2013) Buckling pathways in spherical shells with soft spots. *Soft Matter* 9:8227–8245.
33. Bowick MJ, Cacciuto A, Nelson DR, Travesset A (2006) Crystalline particle packings on a sphere with long-range power-law potentials. *Phys Rev B* 73:024115.
34. Reis PM, Ingale RA, Shattuck MD (2006) Crystallization of a quasi-two-dimensional granular fluid. *Phys Rev Lett* 96(25):258001.
35. Moucka F, Nezbeda I (2005) Detection and characterization of structural changes in the hard-disk fluid under freezing and melting conditions. *Phys Rev Lett* 94(4):040601.